INTERNATIONAL JOURNAL FOR NUMERICAL METHODS IN FLUIDS
Int. J. Numer. Meth. Fluids 2009; **61**:514–535
Published online 13 November 2008 in Wiley InterScience (www.interscience.wiley.com). DOI: 10.1002/fld.1956

A comparative study of GLS finite elements with velocity and pressure equally interpolated for solving incompressible viscous flows

Yongtao Wei[1,*,†] and Philippe H. Geubelle[2]

[1]*Department of Applied Mechanics, College of Architecture and Environment, Sichuan University, Chengdu 610065, People's Republic of China*
[2]*Department of Aerospace Engineering, University of Illinois, Urbana, IL 61801, U.S.A.*

SUMMARY

A comparative study of the bi-linear and bi-quadratic quadrilateral elements and the quadratic triangular element for solving incompressible viscous flows is presented. These elements make use of the stabilized finite element formulation of the Galerkin/least-squares method to simulate the flows, with the pressure and velocity fields interpolated with equal orders. The tangent matrices are explicitly derived and the Newton–Raphson algorithm is employed to solve the resulting nonlinear equations. The numerical solutions of the classical lid-driven cavity flow problem are obtained for Reynolds numbers between 1000 and 20 000 and the accuracy and converging rate of the different elements are compared. The influence on the numerical solution of the least square of incompressible condition is also studied. The numerical example shows that the quadratic triangular element exhibits a better compromise between accuracy and converging rate than the other two elements. Copyright © 2008 John Wiley & Sons, Ltd.

Received 15 July 2008; Revised 25 September 2008; Accepted 1 October 2008

KEY WORDS: incompressible viscous flow; Galerkin/least-squares; finite element method; Newton–Raphson

1. INTRODUCTION

The finite element modeling of incompressible viscous flows can be traced back to the 1970s, with the initial development focused on the simulation of viscous flows with low Reynolds numbers [1–5]. Soon it became apparent that the standard Galerkin finite element method (FEM) formulation, which was very successful in structural analysis, led to numerical instabilities and spurious

*Correspondence to: Yongtao Wei, Department of Applied Mechanics, College of Architecture and Environment, Sichuan University, Chengdu 610065, People's Republic of China.
†E-mail: wyt2119@hotmail.com

Contract/grant sponsor: Chinese Scholarship Council

oscillations when used to solve the incompressible Navier–Stokes equations. In most cases the numerical instabilities are so severe that the solutions either do not converge or become meaningless. The incompressible condition, which makes the pressure field independent of the velocity, has long been recognized as the main source of numerical instability that can appear at low and high Reynolds number. The simplest way to eliminate this instability is to use mixed interpolations (or unequal interpolations) for the velocity and pressure fields, which satisfy the Babuska–Brezzi condition [6, 7] or pass the inf–sup test [8]. For example, for the quadrilateral finite element with bi-quadratic velocity interpolation, a discontinuous linear interpolation or a continuous bi-linear interpolation can be adopted for the pressure solution.

The source of spurious oscillations in the velocity solution is due to the standard Galerkin FEM treatment of the convection term, in which the test and trial functions are similar. This convective instability becomes dominant as the Reynolds number increases. Although this instability can simply be removed by keeping the mesh Reynolds number smaller than two so that convection no longer dominates at an element level, this approach is not practical when simulating complex flows. Initial attempts to eliminate the instability triggered by the convective term were enlightened by the finite difference upwind schemes. The Petrov–Galerkin FEM formulation for advection–diffusion equations, which weighs upwind nodes more heavily than downstream nodes, was implemented by Christie *et al.* [9] for one-dimensional cases and by Heinrich *et al.* [10, 11] for two-dimensional cases. However, this straightforward introduction upwind difference was criticized for excessive crosswind diffusion and low accuracy, especially when the flow is skew to the mesh [12].

A breakthrough in the FEM simulation of incompressible viscous flows was achieved by Brooks and Hughes [13], who established a stabilized and higher-order accurate method based on elements with bi-linear velocity and constant pressure interpolations. The formulation, commonly referred to as the streamline upwind/Petrov–Galerkin (SUPG) formulation, relies on the addition of an artificial diffusion only along the flow direction on the perturbation of the derivatives of the Galerkin weighting functions. Later, Hughes and co-workers introduced a Galerkin/least-squares (GLS) method for Stokes flows [14] and for advection–diffusion equations [15], in which least-squares forms of the residuals, discontinuous between elements, are added to the Galerkin formulation to enhance its stability. The GLS method represents a conceptual simplification of the SUPG method and provides a more systematic approach to remove instabilities in the simulation of the incompressible Navier–Stokes equations. Using linear and bi-linear equal-order interpolations for the velocity and pressure fields, Tezduyar *et al.* [16] derived an SUPG/PSPG (pressure-stabilizing/Petrov–Galerkin) formulation for incompressible viscous flows from the GLS method by neglecting the viscous term's contribution to the weighting functions of the residuals. Soon after that Franca and Frey [17] extended the GLS-stabilized FEM formulation to higher-order interpolations, in which the least squares of both the Navier–Stokes equations and the incompressible condition were taken into account. The GLS and SUPG/PSPG formulations circumvent the Babuska–Brezzi condition and allow for any combination of interpolations for velocity and pressure.

The stabilization parameters used in [17] came from the inverse estimate constants given by Harari and Hughes [18]. Later, Franca and Madureria [19] proposed to calculate the stabilization parameters by solving the eigenvalue problem associated with the inverse estimates, thereby bypassing the cumbersome notion of element length. Hannani *et al.* [20] compared the GLS, SUPG and standard Galerkin formulation with the lid-driven cavity problem under various Reynolds numbers and concluded that GLS formulation was superior to its SUPG counterpart. As the least

DOI: 10.1002/fld

square of the incompressible constraint (LSIC) term was excluded from the GLS formulation studied in [20], this formulation was later referred to as the semi-GLS formulation by Burda *et al.* [21]. For the SUPG/PSPG formulation with LSIC term, Tezduyar and Osawa [22] calculated the stabilization parameters from element matrices and vectors, which automatically accounted for the local length scale, an advection field and the Reynolds number. Besides the SUPG, SUPG/PSPG and GLS formulations, other stabilized FEM for incompressible Navier–Stokes equations have also been proposed, including the third-order upwind FEM proposed by Norio *et al.* [23, 24].

The accuracy and convergence rate of three elements associated with the GLS formulations are compared in this paper in the context of the classical problem of the lid-driven cavity flow already considered by Hannani *et al.* [20] but for a wider range of the Reynolds number. The paper also provides the derivation of the tangent matrices for the GLS FEM. The remainder of the paper is organized as follows: in Section 2, we review the boundary value problem of incompressible Navier–Stokes equations. The FEM relations associated with the GLS-stabilized formulation are presented for two-dimensional cases in Section 3, which also describes how to calculate the stabilization parameters and summarizes the Newton–Raphson iterative algorithm adopted to solve the resulting system of nonlinear equations. Section 4 presents the results of the classical lid-driven cavity flow problem with the Reynolds number up to 20 000. This problem is used to assess and compare the accuracy and convergence performance of the various GLS finite elements. The appendices contain a detailed derivation of the FE equations and the corresponding tangent matrices in a form readily amenable to implementation, including the method of calculating the global second-order derivatives of basis functions.

2. INCOMPRESSIBLE NAVIER–STOKES EQUATIONS

Let us consider an isothermal incompressible viscous flow in a spatial domain Ω with boundary Γ. The governing Navier–Stokes equations are given by

$$\rho\frac{\partial \mathbf{u}}{\partial t}+\rho\mathbf{u}\cdot\nabla\mathbf{u}-\nabla\cdot\boldsymbol{\sigma}=\mathbf{b} \quad \text{in } \Omega \tag{1}$$

$$\nabla\cdot\mathbf{u}=0 \quad \text{in } \Omega \tag{2}$$

where ρ is the constant density, $\mathbf{u}$ is the velocity vector, $\mathbf{b}$ is the body force per unit volume and $\boldsymbol{\sigma}$ is the Cauchy stress tensor given by

$$\boldsymbol{\sigma}=-p\mathbf{I}+2\mu\boldsymbol{\varepsilon}(\mathbf{u}) \tag{3}$$

Here p is the pressure, $\mathbf{I}$ is the second-order identity tensor, μ is the dynamic viscosity and $\boldsymbol{\varepsilon}(\mathbf{u})$ is the strain-rate tensor defined as the symmetric part of the velocity gradient

$$\boldsymbol{\varepsilon}(\mathbf{u})=\tfrac{1}{2}[\nabla\mathbf{u}+(\nabla\mathbf{u})^{\mathrm{T}}] \tag{4}$$

Substituting (2)–(4) into (1) yields the following form of the Navier–Stokes equations:

$$\rho\frac{\partial \mathbf{u}}{\partial t}+\rho\mathbf{u}\cdot\nabla\mathbf{u}-\mu\nabla^2\mathbf{u}+\nabla p=\mathbf{b} \quad \text{in } \Omega \tag{5}$$

DOI: 10.1002/fld

Along different segments of the boundary Γ, Dirichlet or Neumann boundary conditions can be imposed as

$$\mathbf{u}=\mathbf{g} \quad \text{along } \Gamma_g \tag{6}$$

$$\boldsymbol{\sigma}\cdot\mathbf{n}=\mathbf{f} \quad \text{along } \Gamma_f \tag{7}$$

where Γ_u and Γ_f are complementary subsets of Γ, $\mathbf{g}$ and $\mathbf{f}$ are given functions and $\mathbf{n}$ is the outer normal unit vector of Γ_f. The formulation of the incompressible viscous problem is completed by the initial condition on $\mathbf{u}$,

$$\mathbf{u}|_{t=0}=\mathbf{u}_0 \quad \text{in } \Omega \tag{8}$$

where $\mathbf{u}_0$ is a given function of position, which satisfies $\nabla\cdot\mathbf{u}_0=0$.

3. STABILIZED FEM FORMULATION

3.1. Stabilized GLS formulation

Let the computational domain Ω be discretized into a set of elements Ω^e, $e=1,2,\ldots,n_{\text{el}}$, where n_{el} is the number of elements, and let S_u^h and V_u^h be the suitably defined finite-dimensional trial solution and test function spaces for velocity, respectively. Let S_p^h and V_p^h be their counterparts for the pressure, with $S_p^h=V_p^h$. According to Franca and Frey [17], the stabilized GLS finite element formulation of (1) and (2) can be written as follows: find $\mathbf{u}\in S_u^h$ and $p\in S_p^h$ such that, $\forall\delta\mathbf{u}\in V_u^h$ and $\forall\delta p\in V_p^h$,

$$\begin{aligned}
&\int_\Omega \delta\mathbf{u}\cdot\left(\rho\frac{\partial\mathbf{u}}{\partial t}+\rho\mathbf{u}\cdot\nabla\mathbf{u}-\mathbf{b}\right)\mathrm{d}\Omega+\int_\Omega \delta\boldsymbol{\varepsilon}:\boldsymbol{\sigma}\,\mathrm{d}\Omega-\int_{\Gamma_f}\delta\mathbf{u}\cdot f\,\mathrm{d}\Gamma+\int_\Omega \delta p(\nabla\cdot\mathbf{u})\,\mathrm{d}\Omega\\
&\quad+\sum_{e=1}^{n_{\text{el}}}\int_{\Omega^e}\tau\left[\mathbf{u}\cdot(\nabla\delta\mathbf{u})-\frac{\mu}{\rho}\nabla^2\delta\mathbf{u}+\frac{(\nabla\delta p)}{\rho}\right]\cdot\left[\rho\left(\frac{\partial\mathbf{u}}{\partial t}+\mathbf{u}\cdot\nabla\mathbf{u}\right)-\mu\nabla^2\mathbf{u}+\nabla p-\mathbf{b}\right]\mathrm{d}\Omega\\
&\quad+\sum_{e=1}^{n_{\text{el}}}\int_{\Omega^e}\tau_{\text{LSIC}}\rho(\nabla\cdot\delta\mathbf{u})(\nabla\cdot\mathbf{u})\,\mathrm{d}\Omega=0
\end{aligned} \tag{9}$$

Here $\delta\mathbf{u}=0$ along Γ_g and $\delta\boldsymbol{\varepsilon}$ is the strain-rate tensor corresponding to $\delta\mathbf{u}$. The first three integrals in (9) come from the standard Galerkin formulation, i.e. from the virtual velocity principle of (1), while the fourth integral is the weighted residual of (2). The fifth and sixth terms, which involve summations over element integrals, are the least-squares forms of (5) and (2), respectively, and provide the GLS and LSIC stabilizing terms.

If $\mu\nabla^2\delta\mathbf{u}/\rho$ is removed from the fifth term in (9), the GLS formulation reduces to the SUPG/PSPG formulation proposed by Tezduyar and Osawa [22]. Thus, the dot products of the residual of (5) with $\mathbf{u}\cdot\nabla(\delta\mathbf{u})$ and $\nabla(\delta p)$, respectively, give the SUPG and PSPG stabilizing term. As the kinematic viscosity is in most cases of the order of 10^{-3} or less, it is not surprising that the GLS and SUPG/PSPG formulations yield very similar solutions.

DOI: 10.1002/fld

Three ways have been proposed to calculate the GLS stabilization parameter τ. The first approach [17] relies on the inverse estimate constants and provides the following form for τ:

$$\tau = \frac{h_e}{2\|\mathbf{u}\|} \min\{Re, 1\} \tag{10}$$

where h_e is the equivalent element length or element diameter and Re is the element Reynolds number defined as

$$Re = \frac{m_k \rho \|\mathbf{u}\| h_e}{4\mu} \tag{11}$$

The parameters h_e and m_k entering (10) and (11) depend on the element shapes and interpolation order for the approximate velocity field. Harari and Hughes [18] calculated these parameters for rectangular and triangular elements with different interpolation orders. Slightly modified expressions are adopted here. For quadrilateral elements, h_e is defined as the usual element diameter, i.e. it is related to the element area A_e through

$$h_e = 2\sqrt{A_e/\pi} \tag{12}$$

For bi-linear and bi-quadratic quadrilateral elements, m_k is $\frac{1}{3}$ and $\frac{11}{135}$, respectively. Note that the definition of h_e adopted here is different from the more complex form proposed in [18] and can be more easily extended to non-rectangular elements, especially when bi-quadratic interpolation is employed. Furthermore our numerical experiments have shown that, for square elements, replacing h_e given in [18] with (12) yields almost identical solutions. For quadratic triangular elements with mid-nodes equally spaced along straight edges, h_e is given by

$$h_e = 4A_e \Big/ \sqrt{3 \sum_{i=1}^{3} s_i^2} \tag{13}$$

where s_i is the distance from the ith vertex to the triangle's centroid.

Franca and Madureria [19] later proposed a definition for τ free of the element length as

$$\tau = \frac{1}{\sqrt{\lambda_K}\|\mathbf{u}\|} \min\left\{ \frac{\|\mathbf{u}\|\rho}{4\sqrt{\lambda_K}\mu}, 1 \right\} \tag{14}$$

where λ_K, given by Equation (35) in [19], is the largest eigenvalue of the generalized eigenvalue problem associated with the inverse estimate for each element. This definition bypasses the difficulty of defining h_e for different element types. However, in arbitrary Lagrangian–Eulerian formulations, where the mesh of the fluid domain can deform during the analysis, computing λ_K for each element at every load step tends to increase the computation time significantly.

With regards to the LSIC stabilization parameter τ_{LSIC} entering the last term of (9), both [17] and [18] use the same expression:

$$\tau_{\mathrm{LSIC}} = \tau \|\mathbf{u}\|^2 \tag{15}$$

In [22], Tezduyar and Osawa proposed a radically different way to compute these stabilization parameters, in which neither the inverse estimates nor the associated eigenvalue problem are needed. The parameters are instead computed based on the element-level matrices and vectors. For more detailed information, please refer to [22].

DOI: 10.1002/fld

In the present study, which only involves two-dimensional meshes composed of quadrilateral and triangular elements, we adopt relations (12), (13) and (15), which are appropriate as long as the element aspect ratio is not too large.

3.2. FE formulation and the Newton–Raphson iteration

The derivation of the nonlinear FEM equations associated with Equation (9) relies on the following two simplifications. First, only the two-dimensional case is considered here, although the formulation presented hereafter can readily be extended to the fully three-dimensional case. Second, to simplify the notations, we assume that the whole computational domain Ω is divided into only one element; hence, summations over elements in Equation (9) vanish and the elemental equilibrium equations have the same form as the global equilibrium equations.

Let $\mathbf{U}$ and $\mathbf{P}$ be the elemental vectors for velocity and pressure and $\delta\mathbf{U}$ and $\delta\mathbf{P}$ be their variational forms, respectively. The symbol $\dot{\mathbf{U}}$ stands for the elemental local acceleration vector, namely, $\partial\mathbf{U}/\partial t$. Thus, $\mathbf{u}$, $\partial\mathbf{u}/\partial t$, $\delta\mathbf{u}$, p and δp can be expressed as

$$\mathbf{u}=\mathbf{N}\mathbf{U}, \quad \frac{\partial\mathbf{u}}{\partial t}=\mathbf{N}\dot{\mathbf{U}}, \quad \delta\mathbf{u}=\mathbf{N}\delta\mathbf{U} \tag{16}$$

$$p=\mathbf{H}\mathbf{P}, \quad \delta p=\mathbf{H}\delta\mathbf{P} \tag{17}$$

where $\mathbf{N}$ and $\mathbf{H}$ are the interpolation function matrices for velocity and pressure, respectively. As mentioned above, equal-order interpolations for velocity and pressure can be employed in GLS and SUPG/PSPG formulations.

Substituting Equations (16) and (17) into Equation (9), transferring the terms expressed in the form of second-order tensors into the equivalent vector or matrix forms and considering the arbitrariness of $\delta\mathbf{U}$ and $\delta\mathbf{P}$ lead to the following semi-discrete GLS-stabilized FEM formulation:

$$\begin{aligned}\boldsymbol{\Psi}=&\int_\Omega \rho\mathbf{N}^{\mathrm{T}}\mathbf{N}\dot{\mathbf{U}}\,\mathrm{d}\Omega+\int_\Omega \rho\mathbf{N}^{\mathrm{T}}\mathbf{L}\mathbf{u}\,\mathrm{d}\Omega+\int_\Omega \mathbf{B}^{\mathrm{T}}\mathbf{T}\,\mathrm{d}\Omega\\&+\int_\Omega \tau\mathbf{W}^{\mathrm{T}}(\rho\mathbf{N}\dot{\mathbf{U}}+\rho\mathbf{L}\mathbf{u}-\mu\hat{\mathbf{N}}^{\mathrm{T}}\mathbf{U}+\hat{\mathbf{H}}\mathbf{P}-\mathbf{b})\,\mathrm{d}\Omega+\int_\Omega \tau_{\mathrm{LSIC}}\rho\mathbf{B}^{\mathrm{T}}\mathbf{m}\mathbf{m}^{\mathrm{T}}\mathbf{B}\mathbf{U}\,\mathrm{d}\Omega-\mathbf{F}\\=&\mathbf{0}\end{aligned} \tag{18}$$

$$\boldsymbol{\Phi}=\int_\Omega \mathbf{H}^{\mathrm{T}}\mathbf{m}^{\mathrm{T}}\mathbf{B}\mathbf{U}\,\mathrm{d}\Omega+\int_\Omega \tau\hat{\mathbf{H}}^{\mathrm{T}}\left[\mathbf{N}\dot{\mathbf{U}}+\mathbf{L}\mathbf{u}-\frac{\mu}{\rho}\hat{\mathbf{N}}\mathbf{U}+\frac{1}{\rho}\hat{\mathbf{H}}\mathbf{P}-\frac{\mathbf{b}}{\rho}\right]\mathrm{d}\Omega=\mathbf{0} \tag{19}$$

In (18) and (19), $\boldsymbol{\Psi}$ and $\boldsymbol{\Phi}$ denote the imbalance forces corresponding to the momentum equations and incompressible condition, respectively, while $\mathbf{F}$ is the nodal forces equivalent to the external loads:

$$\mathbf{F}=\int_\Omega \mathbf{N}^{\mathrm{T}}\mathbf{b}\,\mathrm{d}\Omega+\int_{\Gamma_f}\mathbf{N}^{\mathrm{T}}\mathbf{f}\,\mathrm{d}\Gamma \tag{20}$$

The various matrices entering (18) and (19), such as $\hat{\mathbf{N}}$ and $\hat{\mathbf{H}}$, are given in Appendix A, while the method to calculate the second-order derivatives of the velocity shape functions with respect to the global coordinates, to be used in (18) and (19) also, is described in Appendix B.

DOI: 10.1002/fld

To complete the discretization of the time-dependent equations (18) and (19), the implicit backward Euler scheme is employed, with the local acceleration at time $t+\Delta t$ expressed as

$$\dot{\mathbf{U}}_{t+\Delta t}=\frac{\mathbf{U}_{t+\Delta t}-\mathbf{U}_t}{\Delta t}=\frac{\Delta\mathbf{U}_{t+\Delta t}}{\Delta t} \tag{21}$$

where Δt denotes a constant time increment. Substituting (21) into (18) and (19) yields the imbalance forces $\boldsymbol{\Psi}_{t+\Delta t}$ and $\boldsymbol{\Phi}_{t+\Delta t}$ at time $t+\Delta t$ as

$$\begin{aligned}\boldsymbol{\Psi}_{t+\Delta t}=&\left(\int_\Omega \rho\mathbf{N}^{\mathrm{T}}\mathbf{N}\,\mathrm{d}\Omega\right)\frac{\Delta\mathbf{U}_{t+\Delta t}}{\Delta t}+\int_\Omega \rho\mathbf{N}^{\mathrm{T}}\mathbf{L}_{t+\Delta t}\mathbf{u}_{t+\Delta t}\,\mathrm{d}\Omega+\int_\Omega \mathbf{B}^{\mathrm{T}}\mathbf{T}_{t+\Delta t}\,\mathrm{d}\Omega\\&+\int_\Omega \tau\mathbf{W}^{\mathrm{T}}_{t+\Delta t}\left(\rho\mathbf{N}\frac{\Delta\mathbf{U}_{t+\Delta t}}{\Delta t}+\rho\mathbf{L}_{t+\Delta t}\mathbf{u}_{t+\Delta t}-\mu\hat{\mathbf{N}}^{\mathrm{T}}\mathbf{U}_{t+\Delta t}+\hat{\mathbf{H}}\mathbf{P}_{t+\Delta t}-\mathbf{b}_{t+\Delta t}\right)\mathrm{d}\Omega\\&+\int_\Omega \tau_{\mathrm{LSIC}}\rho\mathbf{B}^{\mathrm{T}}\mathbf{m}\mathbf{m}^{\mathrm{T}}\mathbf{B}\mathbf{U}_{t+\Delta t}\,\mathrm{d}\Omega-\mathbf{F}_{t+\Delta t}\end{aligned} \tag{22}$$

$$\begin{aligned}\boldsymbol{\Phi}_{t+\Delta t}=&\int_\Omega \mathbf{H}^{\mathrm{T}}\mathbf{m}^{\mathrm{T}}\mathbf{B}\mathbf{U}_{t+\Delta t}\,\mathrm{d}\Omega+\int_\Omega \tau\hat{\mathbf{H}}^{\mathrm{T}}\left(\mathbf{N}\frac{\Delta\mathbf{U}_{t+\Delta t}}{\Delta t}+\mathbf{L}_{t+\Delta t}\mathbf{u}_{t+\Delta t}\right.\\&\left.-\frac{\mu}{\rho}\hat{\mathbf{N}}\mathbf{U}_{t+\Delta t}+\frac{1}{\rho}\hat{\mathbf{H}}\mathbf{P}_{t+\Delta t}-\frac{\mathbf{b}_{t+\Delta t}}{\rho}\right)\mathrm{d}\Omega\end{aligned} \tag{23}$$

To solve the resulting nonlinear equations (22) and (23), the Newton–Raphson method is used at every time step, with the tangent matrices denoted as follows:

$$\mathbf{K}^{UU}_{t+\Delta t}=\frac{\bar{\mathrm{d}}\boldsymbol{\Psi}_{t+\Delta t}}{\mathrm{d}\mathbf{U}_{t+\Delta t}},\quad \mathbf{K}^{UP}_{t+\Delta t}=\frac{\bar{\mathrm{d}}\boldsymbol{\Psi}_{t+\Delta t}}{\mathrm{d}\mathbf{P}_{t+\Delta t}},\quad \mathbf{K}^{PU}_{t+\Delta t}=\frac{\bar{\mathrm{d}}\boldsymbol{\Phi}_{t+\Delta t}}{\partial\mathbf{U}_{t+\Delta t}},\quad \mathbf{K}^{PP}_{t+\Delta t}=\frac{\bar{\mathrm{d}}\boldsymbol{\Phi}_{t+\Delta t}}{\mathrm{d}\mathbf{P}_{t+\Delta t}} \tag{24}$$

The overbar symbol in $\bar{\mathrm{d}}\boldsymbol{\Psi}_{t+\Delta t}$ and $\bar{\mathrm{d}}\boldsymbol{\Phi}_{t+\Delta t}$ denotes that contributions of $\mathrm{d}\tau$ and $\mathrm{d}\tau_{\mathrm{LSIC}}$ due to $\mathrm{d}\mathbf{U}_{t+\Delta t}$ entering the differentiation of $\boldsymbol{\Psi}_{t+\Delta t}$ and $\boldsymbol{\Phi}_{t+\Delta t}$ are neglected in our study. A detailed derivation of these tangent matrices is provided in Appendix C. The Newton–Raphson iterative scheme then takes the familiar form

$$\begin{gathered}{}^{(0)}\mathbf{U}_{t+\Delta t}=\mathbf{U}_t,\quad {}^{(0)}\mathbf{P}_{t+\Delta t}=\mathbf{P}_t\\\begin{bmatrix}{}^{(n)}\mathbf{K}^{UU}_{t+\Delta t} & {}^{(n)}\mathbf{K}^{UP}_{t+\Delta t}\\ {}^{(n)}\mathbf{K}^{PU}_{t+\Delta t} & {}^{(n)}K^{PP}_{t+\Delta t}\end{bmatrix}\begin{bmatrix}\Delta^{(n+1)}\mathbf{U}_{t+\Delta t}\\ \Delta^{(n+1)}\mathbf{P}_{t+\Delta t}\end{bmatrix}=-\begin{bmatrix}{}^{(n)}\boldsymbol{\Psi}_{t+\Delta t}\\ {}^{(n)}\boldsymbol{\Phi}_{t+\Delta t}\end{bmatrix}\\{}^{(n+1)}\mathbf{U}_{t+\Delta t}={}^{(n)}\mathbf{U}_{t+\Delta t}+\Delta^{(n+1)}\mathbf{U}_{t+\Delta t}\\{}^{(n+1)}\mathbf{P}_{t+\Delta t}={}^{(n)}\mathbf{P}_{t+\Delta t}+\Delta^{(n+1)}\mathbf{P}_{t+\Delta t}\end{gathered} \tag{25}$$

DOI: 10.1002/fld

with the left superscript denoting the iteration number. The convergence criteria are written as

$$\frac{\max(\|^{(n)}\boldsymbol{\Psi}_{t+\Delta t}\|, \|^{(n)}\boldsymbol{\Phi}_{t+\Delta t}\|)}{\max(\|^{(0)}\boldsymbol{\Psi}_{t+\Delta t}\|, \|^{(0)}\boldsymbol{\Phi}_{t+\Delta t}\|)} \leqslant \varepsilon \tag{26}$$

where ε is a small positive number, typically less than 10^{-4}.

Neglecting the contribution of $\mathbf{W}_{t+\Delta t}$ to the tangent matrix of $\mathbf{K}^{UU}_{t+\Delta t}$ (the term of $\int_\Omega \tau \mathbf{Q}_{t+\Delta t}\mathbf{N}\,\mathrm{d}\Omega$ in Equation (C8)) does not affect the solution accuracy, but may have a great influence on the convergence rate. This is especially the case for quadrilateral bi-linear and bi-quadratic elements, but apparently much less for quadratic triangular elements.

Although the aforementioned iterative algorithm is derived for the simulation of unsteady flows, it can readily be applied to steady problems as well by using one of two approaches. The first one, referred to as time-dependent approach, consists in applying the loads in a ramped way to the prescribed values over a few time steps and then keeping them constant. The steady-state solution is obtained when the local acceleration $\dot{\mathbf{U}}$ tends to zero. The second, more efficient way, referred to as the time-independent approach, consists in removing all temporal terms in $\boldsymbol{\Psi}_{t+\Delta t}$, $\boldsymbol{\Phi}_{t+\Delta t}$, $\mathbf{K}^{UU}_{t+\Delta t}$ and $\mathbf{K}^{PU}_{t+\Delta t}$, and performing the iteration in (25) directly. In that case, the loads can still be applied in a ramped way to enhance convergence, with t just denoting a fictitious loading time.

Based on the formulation derived above, three 2-D elements with equal-order interpolation for velocity and pressure have been implemented: a bi-quadratic quadrilateral element with 3×3 points Gaussian quadrature scheme (denoted hereafter by QUAD1), a bi-linear quadrilateral element with 2×2 points Gaussian quadrature scheme (QUAD2), and a quadratic triangular element with a seven-point Gaussian quadrature scheme (TRIA). These three elements have been implemented using the object-oriented programming approach proposed in [25–27], with the SuperLU 3.0 library adopted to solve the large, sparse and non-symmetrical system of linear equations resulting from (25).

4. NUMERICAL EXAMPLES

The lid-driven cavity flow problem is often used as a benchmark to test incompressible Navier–Stokes flow solvers. The computational domain consists of a unit square with Dirichlet boundary conditions prescribed along its four sides: a unit horizontal velocity along the upper side and zero velocity along the other three sides. For this problem, the flow Reynolds number is simply defined as the reciprocal of the kinetic viscosity.

Despite its geometrical simplicity, the simulation of the lid-driven cavity flow is challenging because of the existence of recirculation regions in the corners of the cavity, in which the solution changes rapidly, and for the singularities in the pressure field in the upper corners. For a brief review on numerical studies of the lid-driven cavity, refer to [28, 29]. Using a finite difference method in streamfunction and vorticity formulation, Erturk *et al.* [29] solved this problem for Reynolds numbers up to 21 000 on a very fine (600×600) grid. In this section, their results are used as benchmark for our numerical results.

For this steady flow problem, the iteration scheme (25) is carried out using the time-independent approach with the number of load steps chosen by dividing the Reynolds number by 500. The tolerance parameter ε entering (26) is set to 10^{-8} at every load step, which corresponds to an

DOI: 10.1002/fld

absolute value of the residual of the governing equations of the order of 10^{-10} or less. The simulations are performed for four values of the Reynolds number (1000, 5000, 10 000 and 20 000) on four uniform meshes made of 20×20, 30×30, 40×40 and 80×80 QUAD1 elements. The corresponding meshes with the same number of degrees of freedom (DOF) for QUAD2 and TRIA elements are obtained by dividing each QUAD1 element into four QUAD2 elements along its two central lines or two TRIA elements along one of its diagonal, respectively. For reference, the 80×80 mesh yields 25 921 nodes and 77 763 DOF.

Figure 1 presents the computed streamlines (left) and pressure contours (right) obtained with the finest (80×80) mesh with TRIA elements for the four values of the Reynolds number. As expected,

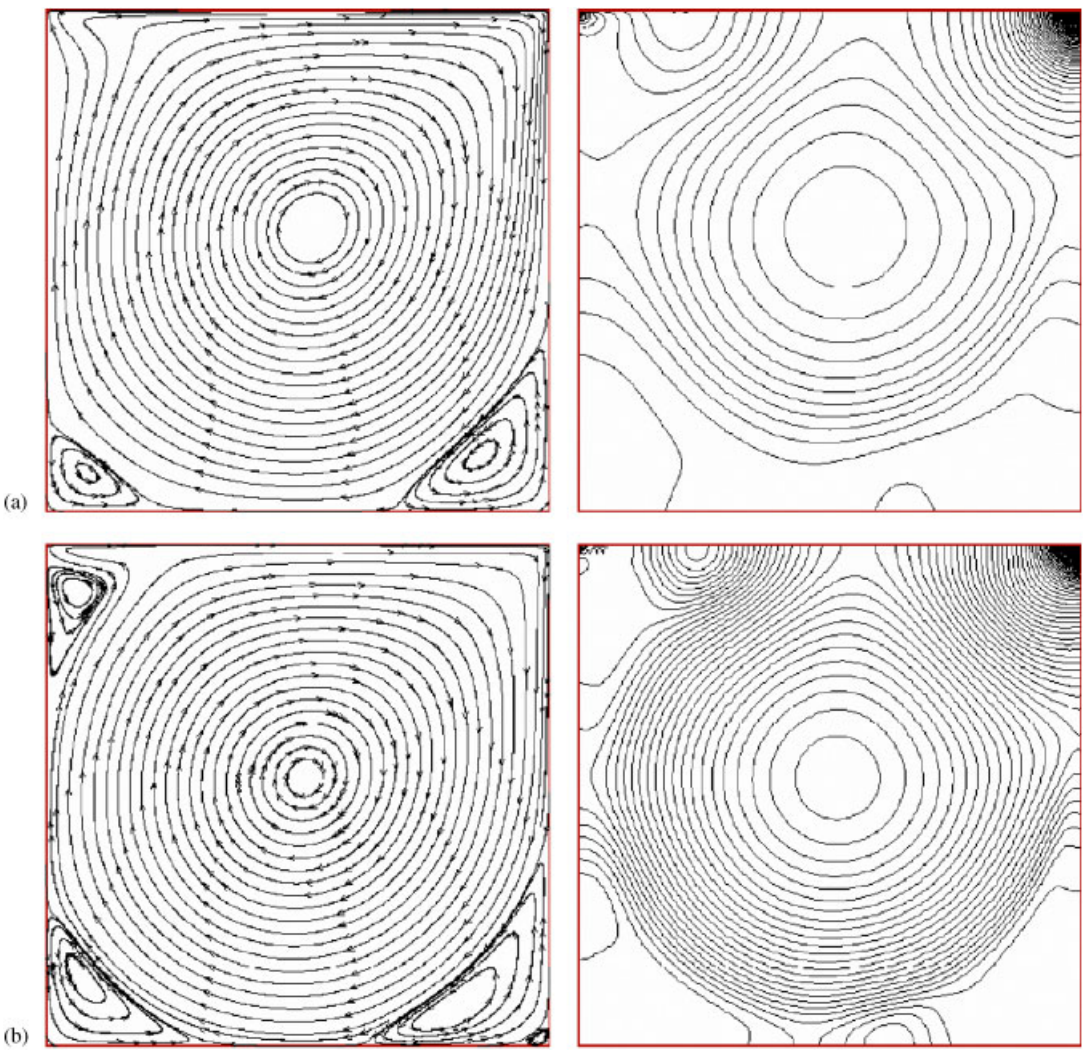

Figure 1. Streamlines (left) and pressure contours (right) for cavity flow with $Re=1000$ (a), 5000 (b), 10 000 (c), and 20 000 (d) obtained on the 80×80 mesh with TRIA elements.

DOI: 10.1002/fld

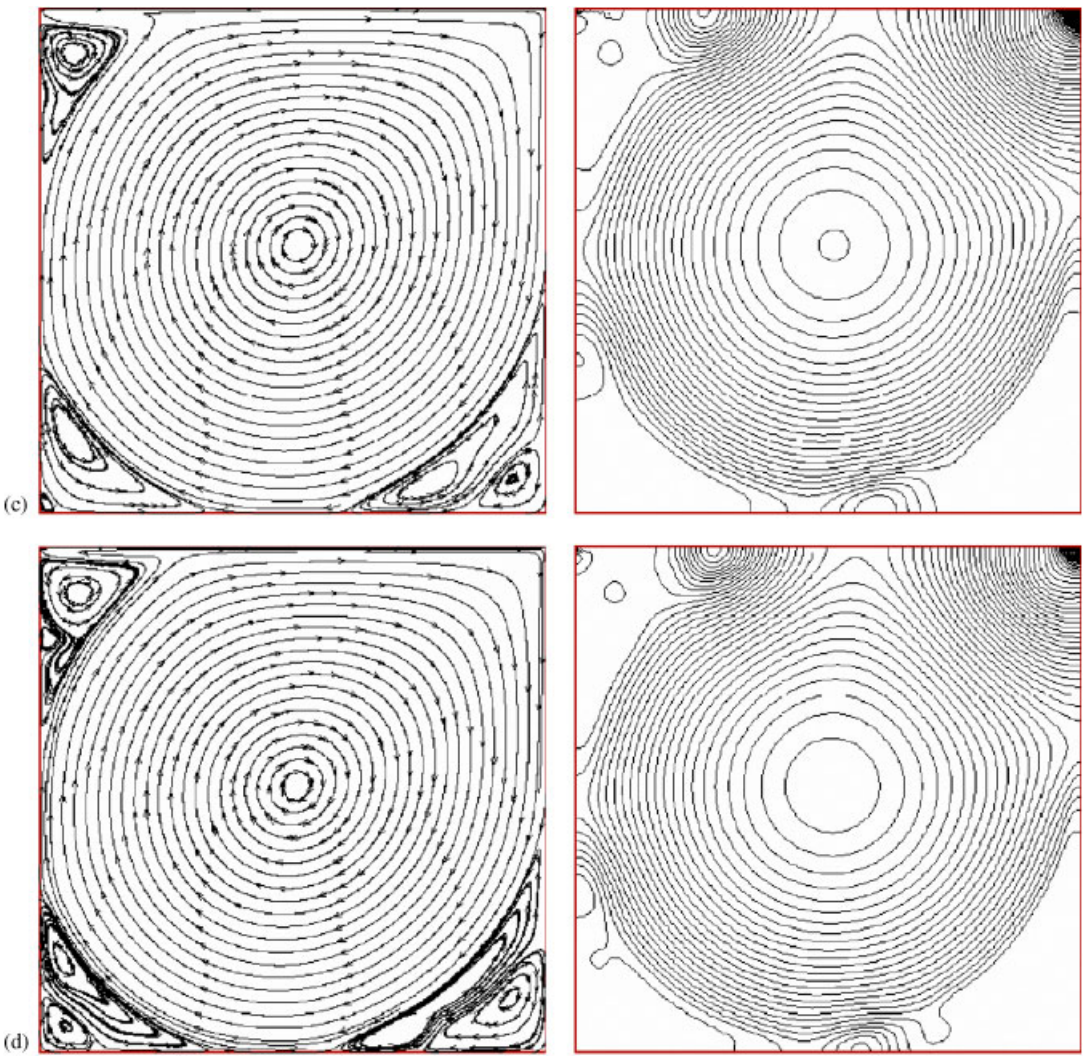

Figure 1. *Continued.*

as Re increases, the amount of recirculation in the corner regions intensifies, with secondary recirculations appearing at $Re > 10\,000$. The pressures contours clearly show the influence of the pressure singularities in the upper corners of the cavity. The 'sharpening' of the velocity gradients is also visible in Figure 2, which presents the spatial variation of the horizontal and vertical velocity components along the vertical and horizontal central lines, respectively, for the two extreme values of the Reynolds number ($Re = 1000$ and $20\,000$). As apparent in that figure, the three element types capture very well the sharp variation of the velocity field in the vicinity of the cavity boundaries, and, except for very small differences near the upper lid at high Reynolds numbers, the numerical solutions compare very well with those obtained with a much finer discretization by

DOI: 10.1002/fld

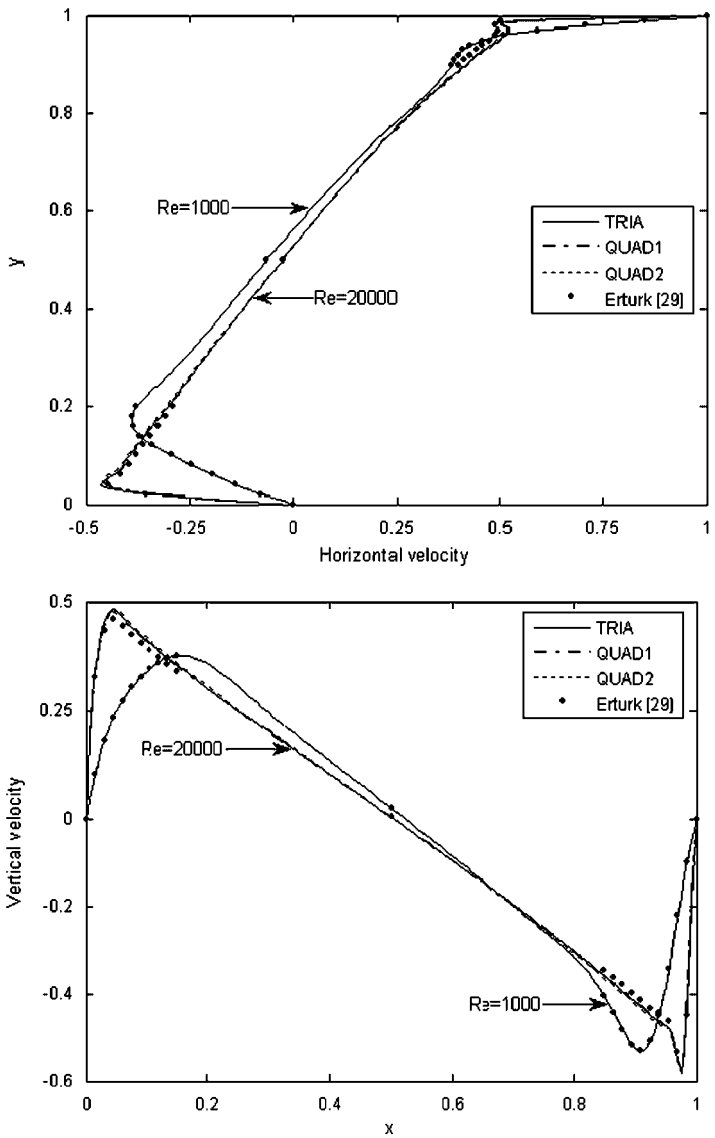

Figure 2. Top: horizontal velocity profile along the vertical central line of the cavity. Bottom: vertical velocity profile along the horizontal central line. Results obtained for $Re = 1000$ and 20 000 on the 80×80 mesh. The symbols denote the benchmark solution obtained by Erturk *et al.* [29].

Erturk *et al.* [29]. Figure 3 presents spatial convergence study for TRIA element type corresponding to $Re = 20\,000$ obtained on three different meshes (20×20, 40×40, 80×80).

To quantify the accuracy of the numerical solutions, we adopt the approach proposed by Aydin and Fenner [30] based on the continuity of the flow. As the net volumetric flow rate passing through the vertical and horizontal central line of the cavity should be equal to zero, we define the flow

DOI: 10.1002/fld

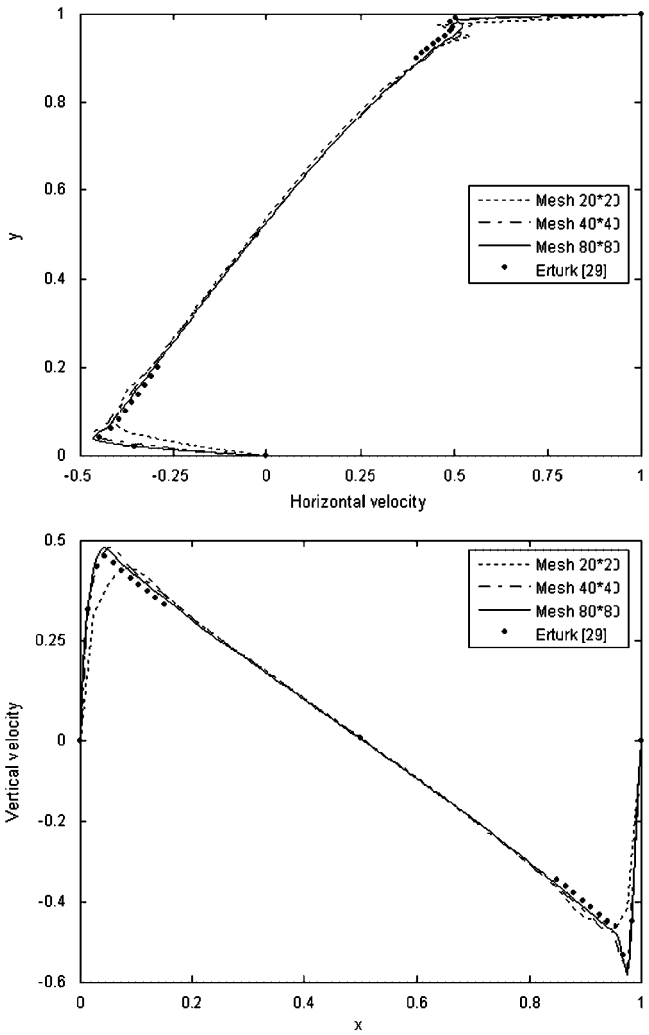

Figure 3. Spatial convergence study: horizontal velocity profile along the vertical central line (top) and vertical velocity profile along the horizontal central line (bottom) corresponding to $Re = 20000$ obtained for three meshes composed of TRIA elements.

rates

$$Q_1 = \left| \int_0^1 u \, dy \right| \Big/ Q_C, \quad Q_2 = \left| \int_0^1 v \, dx \right| \Big/ Q_C \tag{27}$$

where $Q_C = 1.5$ is the horizontal rate corresponding to a linear velocity distribution along the vertical direction. To integrate (27), the Simpson rule is employed for QUAD1 and TRIA elements, and the trapezoidal rule for QUAD2 elements. The dependence of the computed values of Q_1 and Q_2 on the Reynolds number, the mesh size and the element type is presented in

DOI: 10.1002/fld

Tables I–IV. The corresponding values obtained by Erturk *et al.* [29] are also listed for comparison. As apparent from Tables I and II, even on the coarse 20×20 mesh, the computed volume flow rates are very small, with the largest values of Q_1 and Q_2, obtained for the higher Reynolds numbers, of the order of 10^{-4}. As indicated in Tables III and IV, which correspond to the solutions obtained with the 80×80 mesh, the accuracy of the numerical solution is substantially improved by refining the computational mesh. A direct comparison between the results associated with the different element types indicates that the QUAD1 element generally provides the most accurate solutions.

However, as shown in Table V, which compares the CPU time per iteration for the three element types and four mesh sizes, this additional precision comes at a cost, as the computational cost per iteration is substantially higher for the QUAD1 element than for the other two element types. This is due to the fact that the non-symmetric tangent matrix corresponding to that element is more populated than for the other ones, thereby increasing the computational cost of the matrix inversion. Furthermore, as illustrated in Figure 4, the QUAD1 element needs more iterations to achieve the same level of precision as the TRIA and QUAD2 elements. For coarse meshes and high Reynolds numbers, the QUAD1 solution does not converge, as indicated in Tables I and II. As it usually converges faster than the other elements, involves relatively smaller computational cost per iteration and provides the second best accuracy level, the TRIA element-type appears to be the best comprise between accuracy and the 'convergence speed'.

While the introduction of LSIC was described in [21] as 'disastrous', where Taylor–Hood elements of P2P1 or Q2P1 that satisfy the Babuska–Brezzi condition, we do not reach the same conclusion in the present study as the introduction of the LSIC term leads to slightly more accurate solutions (Table VI) without much effect on the convergence rate (Figure 5). While the relatively small impact of that term on the solution might justify its removal, further studies have shown that doing so often leads to divergence of the numerical solution on coarser meshes. For example, when using the TRIA element without the LSIC term to simulate the cavity flow with the Reynolds number 20 000 on a 20×20 mesh, no convergence is achieved, while a convergent

Table I. Volumetric flow rate Q_1 along vertical central line, mesh 20×20.

Reynolds number	TRIA	QUAD1	QUAD2	Erturk *et al.* [29] (600×600 grid)
1000	26.1×10^{-6}	20.4×10^{-6}	342×10^{-6}	0.045×10^{-6}
5000	56.3×10^{-6}	2.83×10^{-6}	258×10^{-6}	0.067×10^{-6}
10 000	38.9×10^{-6}	119×10^{-6}	172×10^{-6}	0.114×10^{-6}
20 000	93.8×10^{-6}	NA	17.6×10^{-6}	0.557×10^{-6}

Table II. Volumetric flow rate Q_2 along horizontal central line, mesh 20×20.

Reynolds number	TRIA	QUAD1	QUAD2	Erturk *et al.* [29] (600×600 grid)
1000	16.2×10^{-6}	7.14×10^{-6}	113×10^{-6}	0.134×10^{-6}
5000	279×10^{-6}	432×10^{-6}	539×10^{-6}	0.693×10^{-6}
10 000	514×10^{-6}	808×10^{-6}	533×10^{-6}	1.34×10^{-6}
20 000	698×10^{-6}	NA	473×10^{-6}	2.35×10^{-6}

DOI: 10.1002/fld

Table III. Volumetric flow rate Q_1 along vertical central line, mesh 80×80.

Reynolds number	TRIA	QUAD1	QUAD2	Erturk *et al.* [29] (600×600 grid)
1000	0.0988×10^{-6}	0.0160×10^{-6}	26.2×10^{-6}	0.045×10^{-6}
5000	1.03×10^{-6}	0.373×10^{-6}	46.0×10^{-6}	0.067×10^{-6}
10 000	1.30×10^{-6}	0.373×10^{-6}	43.7×10^{-6}	0.114×10^{-6}
20 000	3.07×10^{-6}	1.14×10^{-6}	43.0×10^{-6}	0.557×10^{-6}

Table IV. Volumetric flow rate Q_2 along horizontal central line, mesh 80×80.

Reynolds number	TRIA	QUAD1	QUAD2	Erturk *et al.* [29] (600×600 grid)
1000	0.137×10^{-6}	0.0431×10^{-6}	3.17×10^{-6}	0.134×10^{-6}
5000	0.395×10^{-6}	0.00319×10^{-6}	20.3×10^{-6}	0.693×10^{-6}
10 000	0.731×10^{-6}	0.712×10^{-6}	36.4×10^{-6}	1.34×10^{-6}
20 000	1.36×10^{-6}	0.0865×10^{-6}	46.8×10^{-6}	2.35×10^{-6}

Table V. CPU time in seconds per iteration on different meshes.

Mesh	TRIA	QUAD1	QUAD2
20×20	1.15	2.26	0.982
30×30	3.78	6.77	3.26
40×40	8.62	14.3	8.60
80×80	85.6	109	77.6

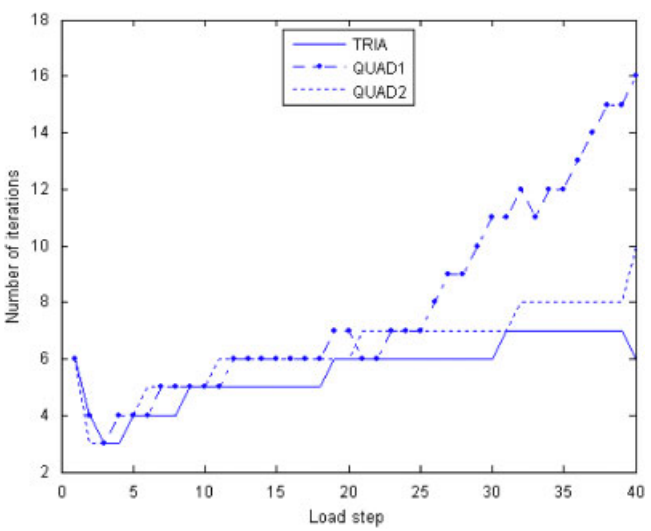

Figure 4. Iteration history for cavity flow with $Re=20000$ and 80×80 mesh.

DOI: 10.1002/fld

Table VI. Effect of an LSIC term on net volumetric flow rate check with TRIA elements.

		Q_1		Q_2	
Reynolds number	Mesh	With LSIC	Without LSIC	With LSIC	Without LSIC
1000	20×20	26.1×10^{-6}	27.2×10^{-6}	16.2×10^{-6}	45.3×10^{-6}
5000	30×30	28.2×10^{-6}	43.5×10^{-6}	41.1×10^{-6}	99.8×10^{-6}
10 000	40×40	18.8×10^{-6}	31.9×10^{-6}	35.7×10^{-6}	124×10^{-6}
20 000	80×80	3.07×10^{-6}	5.53×10^{-6}	1.36×10^{-6}	11.2×10^{-6}

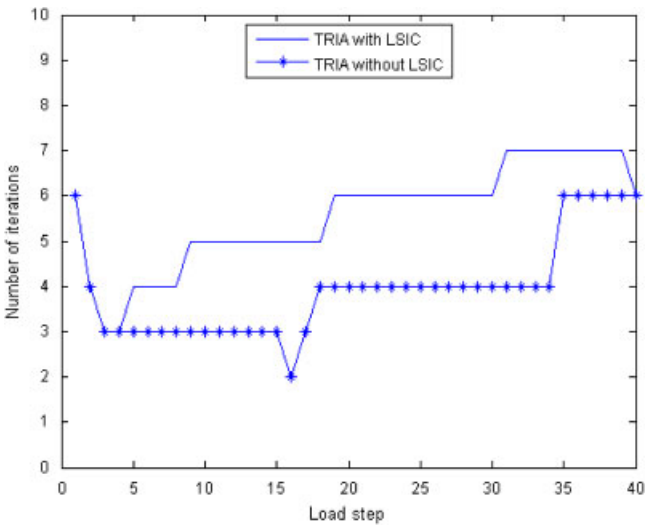

Figure 5. Iteration history for cavity flow solution with and without LSIC ($Re=20\,000$, TRIA elements, 80×80 mesh).

solution, albeit not very precise, can be obtained when the LSIC term is kept. Similar observations have been reached for simulations with QUAD1 and QUAD2 element for the $Re=10\,000$ case on the 20×20 mesh. It appears therefore preferable to keep the LSIC term.

5. CONCLUSION

This paper has summarized the Galerkin/least-squares-stabilized finite element methods for fluid flow problems described by the incompressible Navier–Stokes equations. It also provided the expression of all tangent matrices and residual vectors needed for the Newton–Raphson solution of these equations. Three elements employing equal-order interpolation for velocity and pressure have been tested with the aid of the classical lid-driven cavity flow problem with Reynolds numbers ranging from 1000 to 20 000 solved on various meshes. The accuracy, assessed through the net volumetric flow rate check, and the speed of convergence associated with these three elements

DOI: 10.1002/fld

have been compared. This comparative study has shown that the triangular quadratic element provides an accuracy similar to that of the quadrilateral bi-quadratic element, but is much less computationally intensive in terms of CPU time per iteration and the number of iteration for convergence. When fine meshes are employed, removing the LSIC term reduces the number of iterations with little accuracy loss, but keeping that term alleviates convergence problems on coarse meshes.

APPENDIX A

When equal-order interpolations for velocity and pressure are adopted, the interpolation matrices **N** and **H** take the form

$$\mathbf{N}=[N_1\mathbf{I} \ \ldots \ N_{n_{\text{en}}}\mathbf{I}] \tag{A1}$$

$$\mathbf{H}=[N_1 \ \ldots \ N_{n_{\text{en}}}] \tag{A2}$$

where **I** is the identity matrix, N_i denotes the interpolation basis function or shape function associated with the ith node and n_{en} is the number of nodes in an element ($n_{\text{en}}=4$, 9 and 6 for the QUAD1, QUAD2 and TRIA elements, respectively).

To obtain the FE formulation (18) and (19), the various vector and tensor terms appearing in (9) are expressed the equivalent vector or matrix forms with the aid of (16), (17), (A1) and (A2):

$$\mathbf{u}\cdot\nabla\mathbf{u}=\begin{bmatrix}\dfrac{\partial u_1}{\partial x_1} & \dfrac{\partial u_1}{\partial x_2}\\ \dfrac{\partial u_2}{\partial x_1} & \dfrac{\partial u_2}{\partial x_2}\end{bmatrix}\begin{bmatrix}u_1\\ u_2\end{bmatrix}=\mathbf{L}\mathbf{u}=\mathbf{L}\mathbf{N}\mathbf{U} \tag{A3}$$

$$\begin{aligned}\mathbf{u}\cdot(\nabla\delta\mathbf{u}) &= \begin{bmatrix}\dfrac{\partial\delta u_1}{\partial x_1} & \dfrac{\partial\delta u_1}{\partial x_2}\\ \dfrac{\partial\delta u_2}{\partial x_1} & \dfrac{\partial\delta u_2}{\partial x_2}\end{bmatrix}\begin{bmatrix}u_1\\ u_2\end{bmatrix}=(\delta\mathbf{L})\mathbf{u}=\begin{bmatrix}u_1\dfrac{\partial\delta u_1}{\partial x_1}+u_2\dfrac{\partial\delta u_1}{\partial x_2}\\ u_1\dfrac{\partial\delta u_2}{\partial x_1}+u_2\dfrac{\partial\delta u_2}{\partial x_2}\end{bmatrix}\\ &= \begin{bmatrix}\mathbf{u}\cdot\nabla N_1 & 0 & \ldots & \mathbf{u}\cdot\nabla N_{n_{\text{en}}} & 0\\ 0 & \mathbf{u}\cdot\nabla N_1 & \ldots & 0 & \mathbf{u}\cdot\nabla N_{n_{\text{en}}}\end{bmatrix}\delta\mathbf{U}\\ &= \mathbf{G}\delta\mathbf{U}\end{aligned} \tag{A4}$$

$$\nabla^2\delta\mathbf{u}=\begin{bmatrix}\nabla^2 N_1 & 0 & \ldots & \nabla^2 N_{n_{\text{en}}} & 0\\ 0 & \nabla^2 N_1 & \ldots & 0 & \nabla^2 N_{n_{\text{en}}}\end{bmatrix}\delta\mathbf{U}=\hat{\mathbf{N}}\delta\mathbf{U} \tag{A5}$$

$$\nabla p=\begin{bmatrix}\dfrac{\partial N_1}{\partial x_1} & \cdots & \dfrac{\partial N_{n_{\text{en}}}}{\partial x_1}\\ \dfrac{\partial N_1}{\partial x_2} & \cdots & \dfrac{\partial N_{n_{\text{en}}}}{\partial x_2}\end{bmatrix}\mathbf{P}=\hat{\mathbf{H}}\mathbf{P} \tag{A6}$$

DOI: 10.1002/fld

$$(\nabla\cdot\delta\mathbf{u})(\nabla\cdot\mathbf{u})=\delta\mathbf{U}^{\mathrm{T}}\mathbf{B}^{\mathrm{T}}\mathbf{m}\mathbf{m}^{\mathrm{T}}\mathbf{B}\mathbf{U} \tag{A7}$$

$$\delta\boldsymbol{\varepsilon}:\boldsymbol{\sigma}=\delta\mathbf{U}^{\mathrm{T}}\mathbf{B}^{\mathrm{T}}\mathbf{T} \tag{A8}$$

$$\delta p(\nabla\cdot\mathbf{u})=\delta\mathbf{P}^{\mathrm{T}}\mathbf{H}^{\mathrm{T}}\mathbf{m}^{\mathrm{T}}\mathbf{B} \tag{A9}$$

In (A7)–(A9), $\mathbf{m}=[1\ 1\ 0]^{\mathrm{T}}$, the matrix $\mathbf{B}$ relates the strain-rate vector to the elemental velocity vector,

$$\mathbf{B}=\begin{bmatrix} \dfrac{\partial N_1}{\partial x_1} & 0 & \cdots & \dfrac{\partial N_{n_{\mathrm{en}}}}{\partial x_1} & 0 \\ 0 & \dfrac{\partial N_1}{\partial x_2} & \cdots & 0 & \dfrac{\partial N_{n_{\mathrm{en}}}}{\partial x_2} \\ \dfrac{\partial N_1}{\partial x_2} & \dfrac{\partial N_1}{\partial x_1} & \cdots & \dfrac{\partial N_{n_{\mathrm{en}}}}{\partial x_2} & \dfrac{\partial N_{n_{\mathrm{en}}}}{\partial x_1} \end{bmatrix} \tag{A10}$$

and $\mathbf{T}$ is the vector form of the Cauchy stress tensor defined as

$$\mathbf{T}=[\sigma_{11}\ \ \sigma_{22}\ \ \sigma_{12}]^{\mathrm{T}} \tag{A11}$$

To simplify the notation, let us define the matrix $\mathbf{W}$ as

$$\mathbf{W}=\mathbf{G}-\frac{\mu}{\rho}\hat{\mathbf{N}} \tag{A12}$$

If the SUPG/PSPG formulation is used, $\mathbf{W}$ takes a different form:

$$\mathbf{W}=\mathbf{G} \tag{A13}$$

Extending (18) and (19) to the 3-D case is readily achieved by modifying some of the matrices appearing in these relations, such as $\mathbf{L}$ and $\mathbf{G}$, to the suitable forms, and by adopting the 3-D definition of the stabilization parameter τ.

APPENDIX B

As apparent from (9), the discretization of the GLS and SUPG/PSPG formulations involves the calculation of the second derivatives of the approximate velocity field with respect to the global coordinates. However, since the associated shape functions are usually expressed in the explicit form of the local coordinates, calculating their global second derivatives with respect to the global coordinates is not straightforward. This appendix summarizes the key relations needed to compute these derivatives for an isoparametric formulation, a step seldom included in GLS and SUPG/PSPG papers.

We start from the isoparametric mapping

$$x_1=x_1(\xi,\eta)=\sum_{i=1}^{n_{\mathrm{ne}}}x_1^i N_i(\xi,\eta),\quad x_2=x_2(\xi,\eta)=\sum_{i=1}^{n_{\mathrm{ne}}}x_2^i N_i(\xi,\eta) \tag{B1}$$

where x_1^i and x_2^i are global coordinates of the ith node in an element, and ξ and η are the local coordinates for quadrilateral elements or the independent area coordinates for triangular elements. Provided the inverse transformation of (B1) exists, N_i can also be written as implicit functions of

DOI: 10.1002/fld

x_1 and x_2:

$$N_i(\xi,\eta)=N_i(x_1(\xi,\eta),x_2(\xi,\eta)) \tag{B2}$$

Differentiating (B2) twice with respect to ξ and η and applying the chain rule yield the following relationship between the second-order derivatives of N_i with respect to the local and global coordinates:

$$\begin{bmatrix} \left(\frac{\partial x_1}{\partial \xi}\right)^2 & \left(\frac{\partial x_2}{\partial \xi}\right)^2 & 2\frac{\partial x_1}{\partial \xi}\frac{\partial x_2}{\partial \xi} \\ \left(\frac{\partial x_1}{\partial \eta}\right)^2 & \left(\frac{\partial x_2}{\partial \eta}\right)^2 & 2\frac{\partial x_1}{\partial \eta}\frac{\partial x_2}{\partial \eta} \\ \frac{\partial x_1}{\partial \xi}\frac{\partial x_1}{\partial \eta} & \frac{\partial x_2}{\partial \xi}\frac{\partial x_2}{\partial \eta} & \frac{\partial x_1}{\partial \xi}\frac{\partial x_2}{\partial \eta}+\frac{\partial x_1}{\partial \eta}\frac{\partial x_2}{\partial \xi} \end{bmatrix} \begin{bmatrix} \frac{\partial^2 N_i}{\partial x_1^2} \\ \frac{\partial^2 N_i}{\partial x_2^2} \\ \frac{\partial^2 N_i}{\partial x_1 \partial x_2} \end{bmatrix} = \begin{bmatrix} \frac{\partial^2 N_i}{\partial \xi^2}-\frac{\partial N_i}{\partial x_1}\frac{\partial^2 x_1}{\partial \xi^2}-\frac{\partial N_i}{\partial x_2}\frac{\partial^2 x_2}{\partial \xi^2} \\ \frac{\partial^2 N_i}{\partial \eta^2}-\frac{\partial N_i}{\partial x_1}\frac{\partial^2 x_1}{\partial \eta^2}-\frac{\partial N_i}{\partial x_2}\frac{\partial^2 x_2}{\partial \eta^2} \\ \frac{\partial^2 N_i}{\partial \xi \partial \eta}-\frac{\partial N_i}{\partial x_1}\frac{\partial^2 x_1}{\partial \xi \partial \eta}-\frac{\partial N_i}{\partial x_2}\frac{\partial^2 x_2}{\partial \xi \partial \eta} \end{bmatrix} \tag{B3}$$

In (B3), terms such as $\partial x_i/\partial \xi$ and $\partial^2 x_i/\partial \xi^2$ are directly computed from the mapping relations (B2), while the first-order derivatives with respect to the global coordinates, $\partial N_i/\partial x_1$ and $\partial N_i/\partial x_2$, are obtained through the familiar equation

$$\begin{bmatrix} \frac{\partial x_1}{\partial \xi} & \frac{\partial x_2}{\partial \xi} \\ \frac{\partial x_1}{\partial \eta} & \frac{\partial x_2}{\partial \eta} \end{bmatrix} \begin{bmatrix} \frac{\partial N_i}{\partial x_1} \\ \frac{\partial N_i}{\partial x_2} \end{bmatrix} = \begin{bmatrix} \frac{\partial N_i}{\partial \xi} \\ \frac{\partial N_i}{\partial \eta} \end{bmatrix} \tag{B4}$$

As apparent from relation (B3), one can readily verify that, for bi-linear elements, $\partial^2 N_i^2/\partial x_j^2$ vanishes only when the element shape remains rectangular.

APPENDIX C

To solve nonlinear equations (22) and (23), the Newton–Raphson method is used at every time step. We thus need to compute the tangent matrices of $\mathbf{\Psi}_{t+\Delta t}$ and $\mathbf{\Phi}_{t+\Delta t}$ with respect to $\mathrm{d}\mathbf{U}_{t+\Delta t}$ and $\mathrm{d}\mathbf{P}_{t+\Delta t}$. Although both τ and τ_{LSIC} are relevant to the latest value of $\mathbf{U}_{t+\Delta t}$, their contributions to the tangent matrices are neglected in our study. Differentiating (22) and (23) yields

$$\begin{aligned} \bar{\mathrm{d}}\mathbf{\Psi}_{t+\Delta t} = {} & \frac{1}{\Delta t}\left(\int_\Omega \rho \mathbf{N}^{\mathrm{T}}\mathbf{N}\,\mathrm{d}\Omega\right)\mathrm{d}\mathbf{U}_{t+\Delta t}+\int_\Omega \rho \mathbf{N}^{\mathrm{T}}\,\mathrm{d}\left(\mathbf{L}_{t+\Delta t}\mathbf{u}_{t+\Delta t}\right)\mathrm{d}\Omega+\int_\Omega \mathbf{B}^{\mathrm{T}}\,\mathrm{d}\mathbf{T}_{t+\Delta t}\,\mathrm{d}\Omega \\ & +\frac{1}{\Delta t}\left(\int_\Omega \rho\tau \mathbf{W}^{\mathrm{T}}\mathbf{N}\,\mathrm{d}\Omega\right)\mathrm{d}\mathbf{U}_{t+\Delta t}+\int_\Omega \rho\tau \mathbf{W}^{\mathrm{T}}\,\mathrm{d}(\mathbf{L}_{t+\Delta t}\mathbf{u}_{t+\Delta t})\,\mathrm{d}\Omega \\ & -\left(\int_\Omega \tau\mu \mathbf{W}^{\mathrm{T}}\hat{\mathbf{N}}\,\mathrm{d}\Omega\right)\mathrm{d}\mathbf{U}_{t+\Delta t}+\left(\int_\Omega \tau \mathbf{W}^{\mathrm{T}}\hat{\mathbf{H}}\,\mathrm{d}\Omega\right)\mathrm{d}\mathbf{P}_{t+\Delta t} \\ & +\int_\Omega \tau(\mathrm{d}\mathbf{W}^{\mathrm{T}}_{t+\Delta t})\mathbf{R}_{t+\Delta t}\,\mathrm{d}\Omega+\left(\int_\Omega \tau_{\mathrm{LSIC}}\rho \mathbf{B}^{\mathrm{T}}\mathbf{m}\mathbf{m}^{\mathrm{T}}\mathbf{B}\mathrm{d}\Omega\right)\mathrm{d}\mathbf{U}_{t+\Delta t} \end{aligned} \tag{C1}$$

DOI: 10.1002/fld

$$\bar{\mathrm{d}}\boldsymbol{\Phi}_{t+\Delta t} = \left(\int_\Omega \mathbf{H}^{\mathrm{T}}\mathbf{m}^{\mathrm{T}}\mathbf{B}\,\mathrm{d}\Omega\right)\mathrm{d}\mathbf{U}_{t+\Delta t} + \frac{1}{\Delta t}\left(\int_\Omega \tau\hat{\mathbf{H}}^{\mathrm{T}}\mathbf{N}\,\mathrm{d}\Omega\right)\mathrm{d}\mathbf{U}_{t+\Delta t} + \int_\Omega \tau\hat{\mathbf{H}}^{\mathrm{T}}\mathrm{d}(\mathbf{L}_{t+\Delta t}\mathbf{u}_{t+\Delta t})\,\mathrm{d}\Omega$$
$$-\left(\int_\Omega \frac{\tau\mu}{\rho}\hat{\mathbf{H}}^{\mathrm{T}}\hat{\mathbf{N}}\,\mathrm{d}\Omega\right)\mathrm{d}\mathbf{U}_{t+\Delta t} + \left(\int_\Omega \frac{\tau}{\rho}\hat{\mathbf{H}}^{\mathrm{T}}\hat{\mathbf{H}}\,\mathrm{d}\Omega\right)\mathrm{d}\mathbf{P}_{t+\Delta t} \tag{C2}$$

The overbar in $\bar{\mathrm{d}}\boldsymbol{\Psi}_{t+\Delta t}$ and $\bar{\mathrm{d}}\boldsymbol{\Phi}_{t+\Delta t}$ means that only partial increments due to $\mathrm{d}\mathbf{U}_{t+\Delta t}$ and $\mathrm{d}\mathbf{P}_{t+\Delta t}$ have been taken into account. The term $\mathbf{R}_{t+\Delta t}$ in (C1) is defined as the discretized form of the residual of Equation (5):

$$\mathbf{R}_{t+\Delta t} = \begin{bmatrix} R^1_{t+\Delta t} \\ R^2_{t+\Delta t} \end{bmatrix} = \rho\frac{\partial \mathbf{u}_{t+\Delta t}}{\partial t} + \rho\mathbf{u}_{t+\Delta t}\cdot\nabla\mathbf{u}_{t+\Delta t} - \mu\nabla^2\mathbf{u}_{t+\Delta t} + \nabla p_{t+\Delta t} - \mathbf{b}_{t+\Delta t}$$
$$= \rho\mathbf{N}\frac{\Delta\mathbf{U}_{t+\Delta t}}{\Delta t} + \rho\mathbf{L}_{t+\Delta t}\mathbf{u}_{t+\Delta t} - \mu\hat{\mathbf{N}}^{\mathrm{T}}\mathbf{U}_{t+\Delta t} + \hat{\mathbf{H}}\mathbf{P}_{t+\Delta t} - \mathbf{b}_{t+\Delta t} \tag{C3}$$

To obtain the corresponding tangent matrices, terms of $\mathrm{d}(\mathbf{L}_{t+\Delta t}\mathbf{u}_{t+\Delta t})$, $\mathbf{B}^{\mathrm{T}}\mathrm{d}\mathbf{T}_{t+\Delta t}$ and $(\mathrm{d}\mathbf{W}^{\mathrm{T}}_{t+\Delta t})$ $\mathbf{R}_{t+\Delta t}$ in Equations (C1) should be further expressed as the explicit form of $\mathrm{d}\mathbf{U}_{t+\Delta t}$ and $\mathrm{d}\mathbf{P}_{t+\Delta t}$. Noticing the relationship (A4), we have

$$\mathrm{d}(\mathbf{L}_{t+\Delta t}\mathbf{u}_{t+\Delta t}) = \mathrm{d}(\mathbf{L}_{t+\Delta t})\mathbf{u}_{t+\Delta t} + \mathbf{L}_{t+\Delta t}\mathrm{d}(\mathbf{u}_{t+\Delta t}) = (\mathbf{G}_{t+\Delta t} + \mathbf{L}_{t+\Delta t}\mathbf{N})\mathrm{d}\mathbf{U}_{t+\Delta t} \tag{C4}$$

while the constitutive relation (3) leads to

$$\mathbf{B}^{\mathrm{T}}\mathrm{d}\mathbf{T}_{t+\Delta t} = -\mathbf{B}^{\mathrm{T}}\mathbf{m}\mathbf{H}\mathrm{d}\mathbf{P}_{t+\Delta t} + \mathbf{B}^{\mathrm{T}}\mathbf{C}\mathbf{B}\mathrm{d}\mathbf{U}_{t+\Delta t} \tag{C5}$$

where $\mathbf{C}$ is the constitutive matrix defined in the 2-D case as

$$\mathbf{C} = \begin{bmatrix} 2\mu & 0 & 0 \\ 0 & 2\mu & 0 \\ 0 & 0 & \mu \end{bmatrix} \tag{C6}$$

Whichever form (A12) or (A13) the quantity $\mathbf{W}$ takes, the product $(\mathrm{d}\mathbf{W}^{\mathrm{T}}_{t+\Delta t})\mathbf{R}_{t+\Delta t}$ can be expanded as

$$(\mathrm{d}\mathbf{W}^{\mathrm{T}}_{t+\Delta t})\mathbf{R}_{t+\Delta t} = \begin{bmatrix} \mathrm{d}\mathbf{u}_{t+\Delta t}\cdot\nabla N_1 & 0 \\ 0 & \mathrm{d}\mathbf{u}_{t+\Delta t}\cdot\nabla N_1 \\ \vdots & \vdots \\ \mathrm{d}\mathbf{u}_{t+\Delta t}\cdot\nabla N_{n_{\mathrm{en}}} & 0 \\ 0 & \mathrm{d}\mathbf{u}_{t+\Delta t}\cdot\nabla N_{n_{\mathrm{en}}} \end{bmatrix}\begin{bmatrix} R^1_{t+\Delta t} \\ R^2_{t+\Delta t} \end{bmatrix} = \begin{bmatrix} R^1_{t+\Delta t}(\mathrm{d}\mathbf{u}_{t+\Delta t}\cdot\nabla N_1) \\ R^2_{t+\Delta t}(\mathrm{d}\mathbf{u}_{t+\Delta t}\cdot\nabla N_1) \\ \vdots \\ R^1_{t+\Delta t}(\mathrm{d}\mathbf{u}_{t+\Delta t}\cdot\nabla N_{n_{\mathrm{en}}}) \\ R^2_{t+\Delta t}(\mathrm{d}\mathbf{u}_{t+\Delta t}\cdot\nabla N_{n_{\mathrm{en}}}) \end{bmatrix}$$

DOI: 10.1002/fld

$$= \begin{bmatrix} R^1_{t+\Delta t}\dfrac{\partial N_1}{\partial x_1} & R^1_{t+\Delta t}\dfrac{\partial N_1}{\partial x_2} \\ R^2_{t+\Delta t}\dfrac{\partial N_1}{\partial x_1} & R^2_{t+\Delta t}\dfrac{\partial N_1}{\partial x_2} \\ \vdots & \vdots \\ R^1_{t+\Delta t}\dfrac{\partial N_{n_{\text{en}}}}{\partial x_1} & R^1_{t+\Delta t}\dfrac{\partial N_{n_{\text{en}}}}{\partial x_2} \\ R^2_{t+\Delta t}\dfrac{\partial N_{n_{\text{en}}}}{\partial x_1} & R^2_{t+\Delta t}\dfrac{\partial N_{n_{\text{en}}}}{\partial x_2} \end{bmatrix} \mathbf{N}\mathrm{d}\mathbf{U}_{t+\Delta t} = \mathbf{Q}_{t+\Delta t}\mathbf{N}\mathrm{d}\mathbf{U}_{t+\Delta t} \tag{C7}$$

Substituting (C4)–(C7) into (C1) and (C2) leads to the following form of the tangent matrices:

$$\begin{aligned} \mathbf{K}^{UU}_{t+\Delta t} &= \frac{\bar{\mathrm{d}}\boldsymbol{\Psi}_{t+\Delta t}}{\mathrm{d}\mathbf{U}_{t+\Delta t}} \\ &= \frac{1}{\Delta t}\int_\Omega \rho(\mathbf{N}^{\mathrm{T}} + \tau\mathbf{W}^{\mathrm{T}}_{t+\Delta t})\mathbf{N}\,\mathrm{d}\Omega + \int_\Omega \rho\mathbf{N}^{\mathrm{T}}(\mathbf{G}_{t+\Delta t} + \mathbf{L}_{t+\Delta t}\mathbf{N})\,\mathrm{d}\Omega + \int_\Omega \mathbf{B}^{\mathrm{T}}\mathbf{C}\mathbf{B}\,\mathrm{d}\Omega \\ &\quad + \int_\Omega \tau\mathbf{W}^{\mathrm{T}}_{t+\Delta t}(\rho\mathbf{G}_{t+\Delta t} + \rho\mathbf{L}_{t+\Delta t}\mathbf{N} - \mu\hat{\mathbf{N}})\,\mathrm{d}\Omega + \int_\Omega \tau\mathbf{Q}_{t+\Delta t}\mathbf{N}\,\mathrm{d}\Omega \\ &\quad + \int_\Omega \tau_{\text{LSIC}}\rho\mathbf{B}^{\mathrm{T}}\mathbf{m}\mathbf{m}^{\mathrm{T}}\mathbf{B}\,\mathrm{d}\Omega \end{aligned} \tag{C8}$$

$$\mathbf{K}^{UP}_{t+\Delta t} = \frac{\bar{\mathrm{d}}\boldsymbol{\Psi}_{t+\Delta t}}{\mathrm{d}\mathbf{P}_{t+\Delta t}} = -\int_\Omega \mathbf{B}^{\mathrm{T}}\mathbf{m}\mathbf{H}\,\mathrm{d}\Omega + \int_\Omega \tau\mathbf{W}^{\mathrm{T}}_{t+\Delta t}\hat{\mathbf{H}}\,\mathrm{d}\Omega \tag{C9}$$

$$\begin{aligned} \mathbf{K}^{PU}_{t+\Delta t} &= \frac{\bar{\mathrm{d}}\boldsymbol{\Phi}_{t+\Delta t}}{\partial\mathbf{U}_{t+\Delta t}} \\ &= \int_\Omega \mathbf{H}^{\mathrm{T}}\mathbf{m}^{\mathrm{T}}\mathbf{B}\,\mathrm{d}\Omega + \frac{1}{\Delta t}\int_\Omega \tau\hat{\mathbf{H}}^{\mathrm{T}}\mathbf{N}\,\mathrm{d}\Omega + \int_\Omega \tau\hat{\mathbf{H}}^{\mathrm{T}}\left(\mathbf{G}_{t+\Delta t} + \mathbf{L}_{t+\Delta t}\mathbf{N} - \frac{\mu}{\rho}\hat{\mathbf{N}}\right)\mathrm{d}\Omega \end{aligned} \tag{C10}$$

$$\mathbf{K}^{PP}_{t+\Delta t} = \frac{\bar{\mathrm{d}}\boldsymbol{\Phi}_{t+\Delta t}}{\mathrm{d}\mathbf{P}_{t+\Delta t}} = \int_\Omega \frac{\tau}{\rho}\hat{\mathbf{H}}^{\mathrm{T}}\hat{\mathbf{H}}\,\mathrm{d}\Omega \tag{C11}$$

ACKNOWLEDGEMENTS

The authors gratefully acknowledge the financial support of the Chinese Scholarship Council, which supported W. Y.'s sabbatical leave at the University of Illinois, and the technical assistance of Dr Xiaoye Sherry Li for the incorporation of the SuperLU solver library.

DOI: 10.1002/fld

REFERENCES

1. Cheng RT. Numerical solution of the Navier–Stokes equations by the finite element method. *The Physics of Fluids* 1972; **15**:2098–2105.
2. Baker AJ. Finite element solution algorithm for viscous incompressible fluid dynamics. *International Journal for Numerical Methods in Engineering* 1973; **6**:89–101.
3. Taylor C, Hood P. A numerical solution of the Navier–Stokes equations using the element technique. *Computers and Fluids* 1973; **1**:73–100.
4. Smith SL, Brebbia CA. Finite element solution for Navier–Stokes equation for transient two-dimensional incompressible flow. *Journal of Computational Physics* 1975; **17**:235–245.
5. Kawahara M, Yoshimura N, Nakagawa K, Ohsake H. Steady and unsteady finite element analysis of incompressible viscous fluid. *International Journal for Numerical Methods in Engineering* 1976; **10**:437–456.
6. Babuska I. Error bounds for finite element method. *Numerische Mathematik* 1971; **16**:322–333.
7. Brezzu F. On the existence, uniqueness, and approximation of saddle–point problems arising from Lagrange multiplier. *RAIRO B-R2*, 1974; 129–151.
8. Chapelle D, Bathe KJ. The inf–sup test. *Computers and Structures* 1993; **47**:537–545.
9. Christie I, Griffiths DF, Mitchell AR, Zienkiewicz OC. Finite element methods for second order differential equations with significant first order derivatives. *International Journal for Numerical Methods in Engineering* 1976; **10**:1389–1396.
10. Heinrich JC, Huyakorn PS, Mitchell AR, Zienkiewicz OC. An upwind finite element scheme for two-dimensional convective transport equations. *International Journal for Numerical Methods in Engineering* 1977; **11**:131–141.
11. Heinrich JC, Zienkiewicz OC. Quadratic finite element schemes for two-dimensional convective–transport problems. *International Journal for Numerical Methods in Engineering* 1977; **11**:1831–1844.
12. Gresho PM, Lee RL. Don't suppress the wiggles—They're telling you something. *Computers and Fluids* 1981; **9**:223–253.
13. Brooks AN, Hughes TJR. Streamline upwind/Petrov–Galerkin formulation for convection dominated flows with particular emphasis on the incompressible Navier–Stokes equations. *Computer Methods in Applied Mechanics and Engineering* 1982; **32**:199–249.
14. Hughes TJR, Franca LP. A new finite element formulation for computational fluid dynamics: VII. The Stokes problems with various well-posed boundary condition: symmetric formulation that converge for all velocity/pressure space. *Computer Methods in Applied Mechanics and Engineering* 1987; **65**:85–96.
15. Hughes TJR, Franca LP, Hulbert GM. New finite element formulation for computational fluid dynamics: VIII. The Galerkin/least-square method for advective–diffusive equations. *Computer Methods in Applied Mechanics and Engineering* 1989; **73**:173–189.
16. Tezduyar TE, Mittal S, Ray SE, Shih R. Incompressible flow computations with stabilized bilinear and linear equal-order-interpolation velocity–pressure elements. *Computer Methods in Applied Mechanics and Engineering* 1992; **95**:221–242.
17. Franca LP, Frey SL. Stabilized finite element methods: II. The incompressible Navier–Stokes equation. *Computer Methods in Applied Mechanics and Engineering* 1992; **99**:209–233.
18. Harari I, Hughes TJR. What are C and h: inequalities for the analysis and design of finite element methods. *Computer Methods in Applied Mechanics and Engineering* 1992; **97**:157–192.
19. Franca LP, Madureria AL. Element diameter free stability parameters for stabilized methods applied to fluids. *Computer Methods in Applied Mechanics and Engineering* 1993; **105**:395–403.
20. Hannani SK, Stanislas M, Dupont P. Incompressible Navier–Stokes computation with SUPG and GLS formulation—a comparison study. *Computer Methods in Applied Mechanics and Engineering* 1995; **124**:153–170.
21. Burda P, Novotny J, Sistek J. On a modification of GLS stabilized FEM for solving incompressible viscous flows. *International Journal for Numerical Methods in Fluids* 2006; **51**:1001–1016.
22. Tezduyar TE, Osawa Y. Finite element stabilization parameters computed from element matrices and vectors. *Computer Methods in Applied Mechanics and Engineering* 2000; **190**:411–430.
23. Norio K, Nobuyoshi T, Toshio N. Third-order upwind finite element formulation for incompressible viscous flow problems. *Computer Methods in Applied Mechanics and Engineering* 1991; **93**:169–187.
24. Norio K, Nobuyoshi T, Toshio N. Computation of incompressible viscous flows by the third-order upwind finite element method. *International Journal for Numerical Methods in Fluids* 1992; **15**:1013–1024.
25. Wei YT, Yu JH, Chen JK. Object-oriented approach to the finite element programming: basic data classes. *Journal of Sichuan University* (*Engineering Science Edition*) 2001; **33**(2):17–21.

DOI: 10.1002/fld

26. Wei YT, Yu JH, Chen JK. Object-oriented approach to the finite element programming—design of element procedure. *Journal of Sichuan University* (*Engineering Science Edition*) 2001; **33**(3):9–12.
27. Wei YT, Yu JH, Chen JK. Object-oriented approach to the finite element programming—the application architecture. *Journal of Sichuan University* (*Engineering Science Edition*) 2001; **33**(4):21–25.
28. Shankar PN, Deshpande MD. Fluid mechanics in driven cavity. *Annual Review of Fluid Mechanics* 2000; **32**:93–136.
29. Erturk E, Corke TC, Gokco1 C. Numerical solutions of 2-D steady incompressible driven cavity flow at high Reynolds numbers. *International Journal for Numerical Methods in Fluids* 2005; **48**:747–774.
30. Aydin M, Fenner RT. Boundary element analysis of driven cavity flow for low and moderate Reynolds numbers. *International Journal for Numerical Methods in Fluids* 2001; **37**:45–64.

DOI: 10.1002/fld